Carbon 116 (2017) 264–274

Contents lists available at ScienceDirect

Carbon

journal homepage: www.elsevier.com/locate/carbon

A green and fast approach to nanoporous carbons with tuned porosity: UV-assisted condensation of organic compounds at room temperature

Lavinia Balan [a, **], María C. Fernández de Córdoba [b], Mohamed Zaier [a], Conchi O. Ania [b, *]

[a] CNRS Institut de Science des Matériaux de Mulhouse, UMR 7361, 15 rue Jean Starcky, 68057 Mulhouse Cedex, France
[b] Instituto Nacional del Carbon (INCAR, CSIC), 33011 Oviedo, Spain

ARTICLE INFO

Article history:
Received 29 September 2016
Received in revised form
30 December 2016
Accepted 27 January 2017
Available online 30 January 2017

ABSTRACT

This work reports a green and fast approach to the synthesis of nanoporous carbon materials based on the UV-assisted condensation of organic compounds as precursors. This new approach offers several improvements over the classical soft template and sol-gel routes for the synthesis of materials: versatility of organic precursors, shorter synthesis time, and ambient conditions. Owing to the specificity of the UV-assisted reactions mechanisms, organic compounds of varied chemical composition can be used as precursors in the preparation of nanoporous carbons with tuned porous features. The method consisted in the exposure of an aqueous solution of the organic precursors to UV light for 60 min at room temperature in the absence of a catalyst, allowing an outstanding shortening of the synthesis time compared to sol-gel routes. Furthermore, UV irradiation promoted the cross-linking of the polymer chains of precursors at room temperature, as opposed to classical methods that require an additional step at mild/high temperatures. By changing the chemistry of the organic compound used as precursor, it was possible to modulate the surface area (from 10 to 720 $m^2\ g^{-1}$) and the porosity of the synthesized carbons within the micro-/mesopore range. The obtained carbons also presented varied morphology depending on the precursor, from dense aggregates to ordered hexagonal arrangements of nanometric dimensions.

1. Introduction

Photochemical reactions are those caused by absorption of UV, visible of infrared radiation [1] and many of them occur in nature, such as photosynthesis in plants, human skin production of vitamin D, ozone formation and dissociation in the atmosphere, or photochemical smog (air pollution due to reaction of nitrogen oxides and some volatile organic compounds with sunlight). Most of them proceed through the formation of thermodynamically instable compounds (excited state species usually more reactive than the corresponding ground ones), allowing reactivity otherwise inaccessible by conventional methods [2–4].

In materials' chemistry, photochemical reactions are useful since many molecules and atoms are capable of undergoing chemical changes upon light absorption. Indeed, light-induced transformation of materials is a common phenomenon and the study of light-matter interactions has led to advances in several fields (heterogeneous catalysts, therapeutic applications, patterning of materials for semiconductor applications), and many ground-state reactions have also been studied (e.g. photocycloadditions, photodecarbonylations, photoenolizations, photoisomerizations, photoreductions) [2–6].

Recently, considerable efforts are being devoted to the fabrication of highly featured nanoporous carbon materials with a precise control of their physicochemical, textural and structural properties (uniformity in pore architectures, composition, particle size and shapes), due to their versatility and potential applications in multidisciplinary science and engineering fields (adsorption and separation, catalysis, sensing, energy storage [7,8]. The combination of large specific surface areas (microporosity) and pore volumes along with an adequate network of transport pores (mesopores) is most desirable to favor diffusion and/or adsorption of bulky

* Corresponding author. Current address: CEMHTI, CNRS (UPR 3079), Univ. Orléans, 45071 Orléans, France.
** Corresponding author.
E-mail addresses: lavinia.balan@uha.fr (L. Balan), conchi.ania@cnrs-orleans.fr (C.O. Ania).

http://dx.doi.org/10.1016/j.carbon.2017.01.088

molecules of strategic interest in multidisciplinary fields covering environmental remediation (e.g., hormones, pharmaceuticals, dyes), energy storage and conversion (e.g. electrocatalysis, supercapacitors) and sensing applications (e.g., immobilization of enzymes) [9,10]. In this context, the preparation of nanoporous carbons with well-defined pore architectures in the full micro-/mesopore range has become a subject of great interest. Porous carbon materials typically have relatively broad pore-size distributions, being the porosity mainly dominated by the micropore structure with classical methods showing almost no control over the porous features of the resulting carbons [11,12]. The control over the porous features of the carbons can be achieved to a certain extent by means of nanocasting procedures (soft and hard templating), self-assembling and sol-gel polycondensation reactions, among most representatives [13–16]. However, these are usually time consuming and complex reactions, therefore with quite scarce impact in the large-scale production and commercialization perspectives.

Recently, the use of light-induced reactions has become an interesting tool for the preparation and modification of carbon materials. For instance, Cao et al. showed a localized photothermal growth of carbon nanotubes and silicon nanowires on metal nanoparticles exposed to a focused light beam [17] due to the heat generated at the metallic surface plasmons exposed to irradiation. The same principle based on the light absorption properties of a metallic component has been used to induce the phase transformation of amorphous carbon deposited on nanoparticulated metal films, thereby obtaining carbon materials with enhanced electrical properties (graphitization) [18]. Vinu et al. reported the photofunctionalization of a carbon matrix with carboxylic moieties by exposing the sample to UV light and oxygen at room temperature [19]. The preparation of ordered porous carbons using phloroglucinol as precursor based on photoinduced evaporation reactions has also been reported [20] using a triblock copolymer as sacrificial template. The main advantage of the photoinduced synthesis, compared to the conventional endotemplating route (using the same precursors) is the time scale, since the aging step needed to induce the cross-linking of the polymeric precursor is significantly reduced due to the energy provided by the UV irradiation. Here, we demonstrate a fast and highly localized phase transformation of polyhydroxylated aromatic precursors on liquid phase by irradiation through condensation and spinodal decomposition of the precursor mixtures, to render aromatic resins and ultimately nanoporous carbons after a thermal treatment at 600 °C. We highlight the critical role of the polymeric precursors used in the homogenous liquid phase in bringing about a well connected network, sufficiently cross-linked to render a nanoporous carbon solid after densification of the resin. The difference in yields and porosity of the phenolic resins upon the pyrolytic treatment clearly demonstrates the role of the precursor on the photoassisted phase transformation and cross-linking of the polymers. Changes in composition, nanotexture and microstructure of the materials obtained after irradiation of the precursors were evaluated using Raman spectroscopy, solid state NMR and gas adsorption of several probes at various temperatures.

2. Experimental

2.1. Chemicals

Gallacetophenone (GA), 2,3-dihydroxynaphtalene (DN), pyrogallol (PG) and bisphenol A (BP), Pluronic F127 (poly(ethylene oxide)-block-poly(propylene oxide)-block-poly-(ethylene oxide, $PEO_{106}PPO_{70}PEO_{106}$, M*w* = 12 600 Da), glyoxal aqueous solution (40%, $C_2H_2O_2$), absolute ethanol (C_2H_6O), and HCl (37%) were purchased from Sigma-Aldrich. The chemicals were used as received without any further purification.

2.2. Synthesis

GA, DN, PG and BP were selected as polymeric precursors for the photoassisted synthesis of nanoporous carbons. In a typical synthesis, the precursors (1.6 g) and the surfactant (3.2 g) were dissolved in ethanol containing HCl (37%). After complete dissolution at room temperature, a certain amount of glyoxal (1.6 mL) aqueous solution was added. Afterwards, the solutions were transferred to glass dishes and exposed to UV light for various periods (i.e., up to 70 min). The light source was a lightning cure device fitted with a 365 nm elliptical reflector. An anticaloric filter was used to avoid heating and evaporation during irradiation (monitored temperature was constant). The progress of the photoassisted reaction was monitored via UV–visible absorption spectroscopy using a Thermo Fisher Scientific Evolution 200 spectrophotometer.

The brownish viscous solids obtained after the irradiation were recovered from the dishes and further pyrolyzed at 600 °C under inert atmosphere (i.e., 120 ml/min Ar, heating rate 2°C/min, dwelling time 2 h) to allow the decomposition of the organic resins in carbon materials, and the generation of porosity. The nomenclature assigned for the resins after UV exposure is MM, where MM stands for the organic precursor (GA, PG, BP, DN); when the resins are carbonized, the nomenclature is MM-c600. To evaluate the eventual cross-linking of the organic precursors in the absence of UV light, blank reactions in were carried out for all the studied precursors (allowing the reaction to occur under darkness for several days).

2.3. Characterization techniques

The porosity of all the samples was determined by means of N_2 adsorption/desorption isotherms at −196 °C in a volumetric analyzer (Micromeritics). Before the experiments, the samples were outgassed at 120 °C for 17 h under vacuum (10^{-4} Torr). The specific surface area, S_{BET} and total pore volume, V_{total}, were calculated from the N_2 adsorption data. The pore size distribution in the full micro-/mesopore range was calculated from the N_2 adsorption isotherms using the 2D-NLDFT-HS (www.NLDFT.com) model assuming surface heterogeneity of carbon pores [21]. This model has been validated for the characterization of nanoporous carbons with similar porous features [21–23], and was chosen following IUPAC recommendations to use advanced methods based on NLDFT for the determination of pore size distributions of nanoporous carbons, rather than BJH method that underestimates the pore size for narrow mesopores [24]. The narrow microporosity was further assessed by CO_2 adsorption isotherms at 0 °C using the Dubinin-Radushkevich (DR) equation. All the gases were supplied by Air Products with ultrahigh purity (i.e., 99.995%).

Raman spectroscopy was performed by excitation with green laser light (532 nm) in the range between 1000 and 2000 cm^{-1} (InVia Raman Microscope, equipped with a Leica microscope). The samples were scanned between 10° and 90° (2θ) at a 0.02°/12 s scan rate.

Samples were chemically characterized by elemental analysis. The determination of carbon, hydrogen and nitrogen was carried out by a LECO CHNS-932 and oxygen was measured in a LECO VTF-900 CHNS-932 microanalyzer.

The surface pH of the carbon samples was measured in an aqueous suspension containing 0.4 g of carbon sample powder added to 20 mL of distilled water. After equilibration under stirring overnight, the pH value was measured using a glass electrode.

Thermogravimetric (TG) curves of all the samples were obtained

using a Setaram instrument thermal analyzer (Labsys), under a constant argon flow (100 mL/min). From the TG curves, differential TG (DTG) curves were derived.

The materials were also analyzed by transmission electron microscopy (TEM) with a Philips CM200 instrument working at 200 kV.

X-ray photoelectron spectroscopy (XPS) analysis was performed on a VG Scienta (Uppsala, Sweden) SES 200-2 X-ray photoelectron spectrometer under ultra-high vacuum ($P < 10^{-9}$ mbar). The spectrometer resolution at the Fermi level is about 0.4 eV. The depth analyzed extends up to about 8 nm. The monochromatized AlKα source (1486.6 eV) was operated at a power of 420 W (30 mA and 14 kV) and the spectra of dried powdered samples were acquired at a take-off angle of 90° (angle between the sample surface and photoemission direction). During acquisition, the pass energy was set to 100 eV for high-resolution and 500 eV for wide scan spectra. During the processing of the XPS spectra, energy values were referenced to the C 1s peak of adventitious carbon located at 284.6 eV. CASAXPS software (Casa Software Ltd, Teignmouth, UK, www.casaxps.com) was used for acquisition and data analysis. A Shirley-type background was subtracted from the signals. Recorded spectra were always fitted using Gauss–Lorentz curves, in order to determine the binding energy of the different element core levels more accurately. The error in binding energy was estimated to be ca. 0.1 eV.

Solid-state ^{13}C CP/MAS NMR spectra of the carbonized resins were recorded at room temperature on a Bruker UltraShield Avance 400 spectrometer at 100 MHz. The CPMAS ^{13}C NMR experiments were run using a Bruker 4 mm double-resonance probe head at a spinning speed of 12 kHz. The cross-polarization contact time was 1 ms with a relaxation time of 5 s. The number of transients per spectrum was set to 2000, the acquisition time to 0.034 s, and the spectral width to 18500 Hz. The chemical shift of this signal was also employed to calibrate the shift of the aromatic signal, being 132.1 ppm from tetramethylsilane, and the p/2 pulse width (8.4 ms).

3. Results and discussion

3.1. Photo-assisted synthesis

The photoassisted approach described herein involves the UV irradiation of the precursors' mixture in liquid phase. Fig. 1 shows the UV-VIS spectra of the pristine organic precursor solutions before and after UV exposure at different times (see also Electronic Supplementary Information, Figs. S1 and S2). All the initial solutions of the reactants mixture present absorption between 300 and 400 nm, hence display absorption at the wavelength of the irradiation source used for the photopolymerization reaction (i.e., 365 nm). As the mixtures were exposed to UV light, the solutions progressively darkened, indicating that photoassisted reactions have started (likely polymerization and/or photooxidation of the precursor). Furthermore, the absorbance gradually increased with the irradiation time, indicating that the light favors the self-assembling of the –OH moieties of the hydroxylated precursors and glyoxal. Also, the polymerization rate increased with light (and hence the self-assembly rate). In all the cases the solutions gradually darkened with the illumination time, being this effect less pronounced in the case of gallacetophenone (Fig. 1). Furthermore, for all the organic compounds used as precursors, the solutions underwent spinodal decomposition forming a brownish solid (resin) after 60 min. Since an anticaloric filter was used to avoid the overheating and evaporation of the solutions during UV irradiation, the solid formed after 60 min irradiation is due to the UV-assisted cross-linking of the reactants. Longer exposures (i.e., 70 min) did not modify the mass yield or spectroscopic properties of the solutions (in terms of absorbance), thus 60 min was chosen as optimized light exposure time. The obtained solids were recovered (scratched-out) from the glass dishes and analyzed (no need for solvent evaporation or further thermopolymeration). The eventual cross-linking of the organic precursors in the absence of UV light was evaluated by allowing the reaction of the precursors mixtures in the dark for several days at room temperature. The lack of color changes in the solutions -only a slight darkening for pyrogallol due to its oxygen sensitivity and propensity for self-oxidation [25]-, and of evidences for the formation of a solid phase (Fig. S3) confirmed that the cross-linking of the precursors does not occur in the dark.

Fig. 2 shows the thermogravimetric profiles (DTG curves) under inert atmosphere of the resins retrieved after UV irradiation of the precursors, to evaluate their thermal stability. The corresponding data of the as-received precursors (before UV exposure) is shown in Fig. S4 for comparison purposes. All the samples with the exception of gallacetophenone displayed one peak in the DTG profiles; for all of them, the peak corresponding main mass loss appears at higher temperature (ca. between 300 and 400 °C) than those of their corresponding organic precursors (ca. 200–300 °C), confirming the higher stability of the resins after the photopolymerization reaction. It is important to point out that the thermal profiles of all the precursors (Fig. S4) also displayed a single weight loss (similarly to the resins), despite their different composition. This indicates that the different structural motifs (i.e., hydroxyl and ketone moieties) of the organic precursors do not give rise to multi-stepped profiles, with differences only observed in the overall decomposition temperature (i.e., thermal stability).

In the case of the resin prepared using gallacetophenone, the DTG curve shows a hump at around 250 °C; the temperature of this peak is still higher than that of the as-received organic compound (ca. below 230 °C, see Fig. S4). Interestingly, the profile of the thermal decomposition of gallacetophenone showed only one broad peak (Fig. S4), despite the two structural motifs (i.e., hydroxyl and ketone moieties) of this compound. Thus, data suggests a different polymerization mechanism in this precursor, with the matrix of the resin displaying two moieties with different thermal stability, sufficiently separated to avoid an overlapping of the signal in the thermal profile.

For all the samples the decomposition of the volatile matter is almost complete above 500 °C as the mass loss remained almost unchanged at higher temperatures, thus 600 °C was the selected temperature for the synthesis of the carbons (via densification or pyrolysis).

3.2. Carbon materials

Table 1 shows the yields of carbonization of the photopolymerized resins after the carbonization at 600 °C to obtain the carbonaceous solids. The values differ depending on the precursor, ranging from 9 wt.% in the case of the resin prepared from gallacetophenone, to 24 wt% for pyrogallol. In any case, the yields of carbonization are of the same order of magnitude of the carbonization of polysaccharides, biomass, and other similar precursors with low carbon yields [26]. If the carbon content in the solids after carbonization measured by elemental analysis is recalculated versus the amount of carbon used in the synthesis (Table 1), a clear densification is obtained for all the samples, particularly in the case of gallacetophenone and pyrogallol (suggesting a higher cross-linking degree of the organic precursors). Interestingly, gallacetophenone solution showed a less notorious darkening upon UV irradiation (Fig. 1 and Fig. S2), pointing out to differences in the cross-linking rate of the precursors. This is also in agreement with the two peaks in the DTG profile (Fig. 2A) observed for this sample,

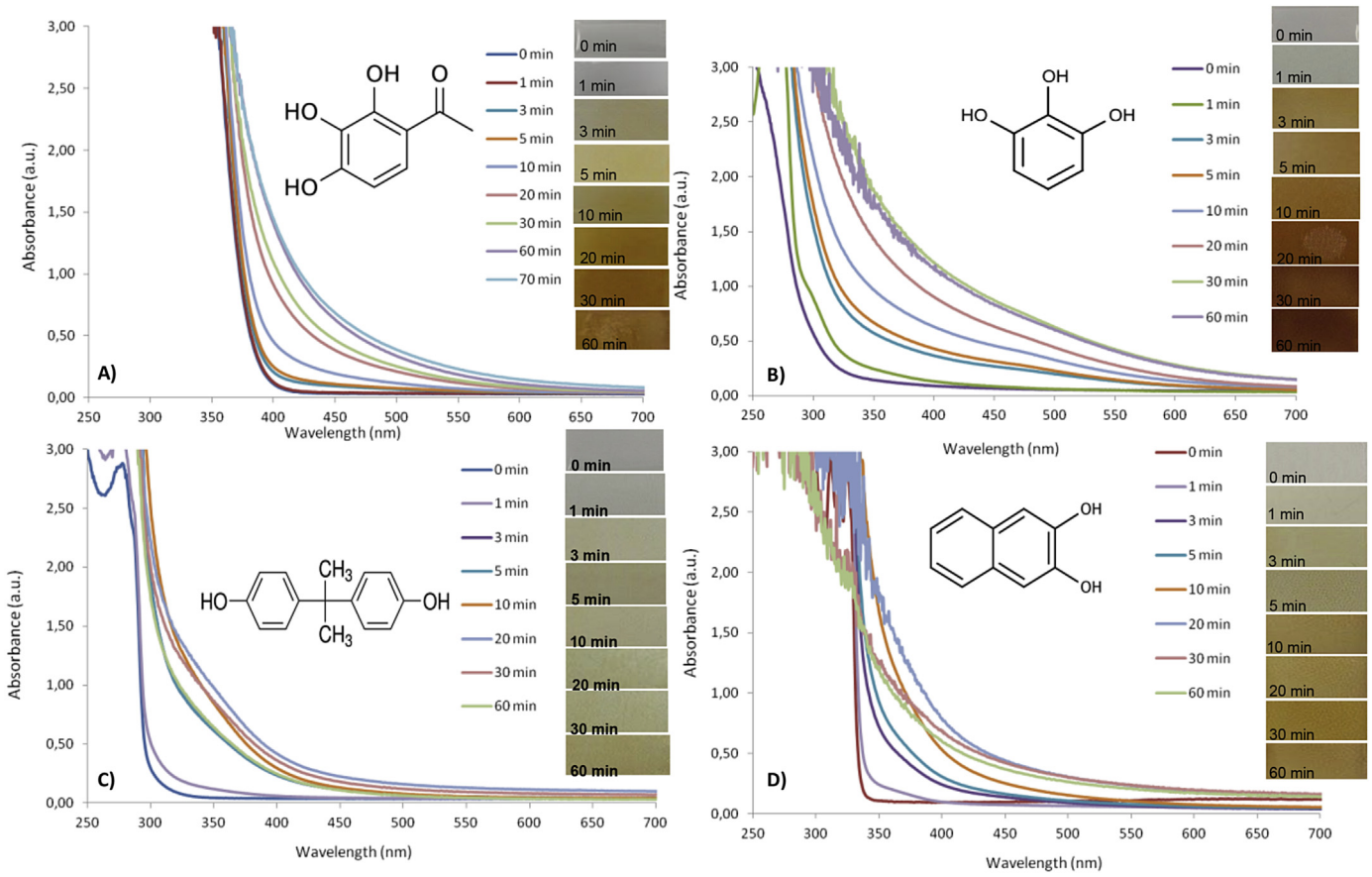

Fig. 1. Evolution of the UV-VIS spectra of the reactants mixtures with UV irradiation time for the different organic precursors: A) Gallacetophenone (GA); B) pyrogallol (PG); C) bisphenol A (BP), and D) 2,3-dihydroxynaphtalene (DN). (A colour version of this figure can be viewed online.)

suggesting that the lower cross-linking of this reactant would also affect the thermal stability of the obtained resin, in terms of lower carbonization yield. On the other hand, there is no clear correlation between the carbonization yields and other parameters such as the molecular weight of the precursors, their thermal stability (Fig. S4) or their functionalization.

The DTG curves of the solids after carbonization at 600 °C (Fig. 2B) were quite similar for all the precursors, but significantly different from those of the photopolymerized resins. The main mass loss occurred above 600 °C and is attributed to the decomposition of volatile matter still remaining on the solids after the carbonization (since the materials were stabilized at this temperature) and/or to the decomposition of the O-surface functionalities anchored in the carbon matrix.

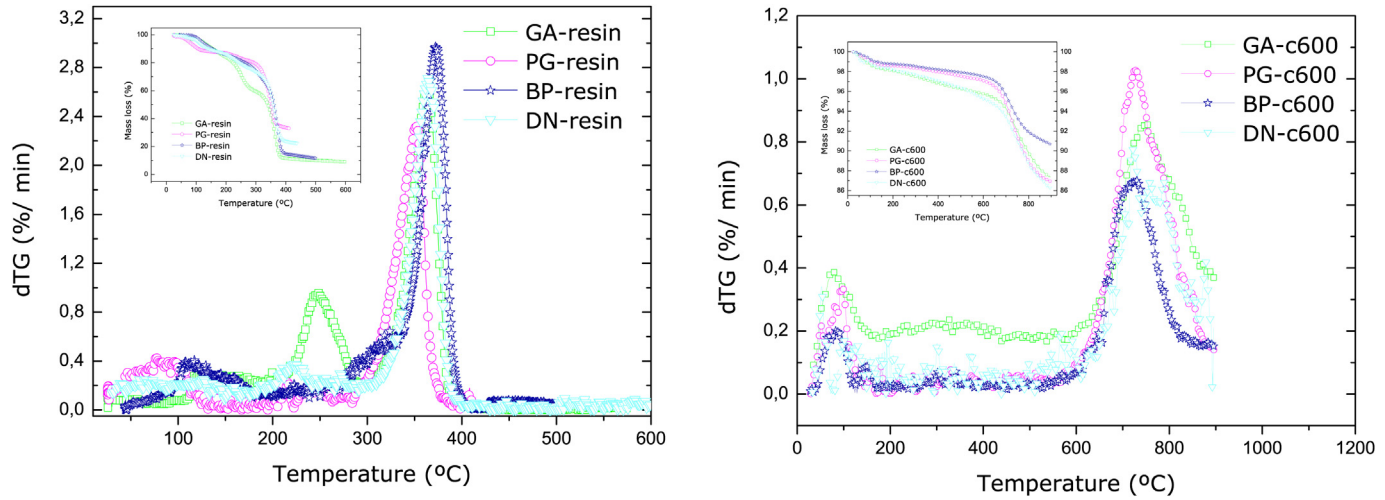

Fig. 2. Thermogravimetric profiles (DTG curves) under inter atmosphere of the photopolymerized resins before (left, series MM-resin) and after carbonization at 600 °C (right, series MM-c600). Insets show the corresponding mass losses. (A colour version of this figure can be viewed online.)

The chemical composition of the samples was analyzed by elemental analysis. The obtained materials exhibited moderate oxygen contents (Table 1), indicating the incorporation of O-groups in the carbonaceous matrix during the UV exposure and/or carbonization steps. Despite the oxygen content, the surface pH of the samples was rather basic, characteristic of hydrophobic carbon materials [27], suggesting that the oxygen is predominantly incorporated in the form of quinone, ether and/or O-bridge (groups of basic nature). Further information about the composition of the carbonized samples was obtained by XPS. The atomic concentrations of the surface elements are also provided in Table 1, and the relative distributions of the different species obtained by deconvolution of the C1s and O1s core level peaks of XPS spectra are shown in Fig. 3 (raw data and fitting of all the samples can be found in Fig. S5 and Table S1).

The amount of surface oxygen follows the trend: GA < DN < BP < PG, and the trend is similar to that obtained from elemental analysis (accounting for the oxygen content in the bulk). The results indicate a higher retention of oxygen in the samples prepared from the carbonization of GA and PG, which seems reasonable considering that both organic precursors present higher oxygen groups that are expected to be incorporated to the carbon matrix during the cross-linking reactions and/or carbonization. The C 1*s* core level spectrum was deconvoluted to various contributions (Fig. S5). The intense peak at 284.5 eV was assigned to carbon in sp^2 configurations, and the contributions at 286.3, 287.3 and 288.5 eV were assigned to phenolic and/or ether (C–OH and C–O–C), carbonyl (C=O) and carboxylic groups (O=C–O), respectively.

As seen in Fig. 3, for all the samples the majority of carbon is in C–C configurations and ca. 3–6% in oxidized forms in various oxygen environments. In addition, the O 1*s* core level broad peaks were decomposed in three contributions at 530.6–531.9 eV, 532.2–533.9 and 533.7–535 eV, assigned to carbonyl, phenol/epoxy, ether and carboxyl, water or chemisorbed oxygen species, respectively [28] (Fig. 3). The oxygen is predominantly in hydroxyl, epoxy and/or ether-like configurations, with equal distributions for all the samples. To further look into the influence of the precursor on the structure of the obtained carbons, the porosity was analyzed. The nitrogen adsorption isotherms, pore size distributions and the summary of the parameters of the pore structure are presented in Fig. 4 and Table 2, respectively.

With the exception sample BP-c600, all the samples can be considered as nanoporous materials, indicating the formation of porosity during the thermal treatment at 600 °C as a result of the decomposition of the volatile matter of the resins. It must be emphasized that no polymerization occurred when the solutions were kept in the dark at room temperature for at least 40 days. Likewise, the thermal heating of the solutions at 50 °C in the dark for 60 min provoked the evaporation of the solvent, without evidence for the cross-linking of the precursors (Fig. S3). This observation excludes the intervention of any important effect in the dark and at room temperature. In the case of BP-c600, the N_2 uptake at −196 °C was negligible; this feature could be due to either poor textural development of this sample, or the presence of narrow micropores through which the diffusion of the gas at cryogenic temperatures is restricted. The latter was confirmed by CO_2 adsorption isotherms at 0 °C [29] (Fig. S6), using the DR method and Stoeckli-Ballerini equation to calculate the narrow micropore volume ($W_{o,CO2}$) and the average micropore size (L), respectively (Table 2).

We observed that, as a general trend, all the samples displayed similar volumes of narrow micropores with average pore sizes of ca. 0.6 nm. Thus, the porous structure of BP-c600 was composed of micropores of small dimensions not accessible to nitrogen. The rest of the samples of the series displayed high N_2 uptakes at -196 °C with important differences between them. For instance, sample DN-c600 has a type I(a) nitrogen adsorption isotherms according to the IUPAC classification [24], characteristic of microporous materials; the marked knee of the isotherm at relative pressures below 0.1 and the reversibility of the isotherm over the entire pressure range, indicates that the porosity is composed of micropores of small sizes with an almost negligible contribution of mesopores. In contrast, samples GA-c600 and PG-600 displayed type IV(b) nitrogen adsorption isotherms, and capillary condensation is accompanied in both cases by marked hysteresis loops indicating the occurrence of mesopores wider than 4 nm [30].

In the case of GA-c600, the hysteresis loop (type H2) expands over the range 0.64–0.98, with smooth almost parallel adsorption/desorption branches over the gas uptake, typically found in complex pore structures in which the desorption path is dependent on network effects (pore-blocking or cavitation induced evaporation) and thus the desorption mechanism is dictated by the pore neck size. The almost parallel adsorption/desorption branches over the gas uptake indicate a narrow range of uniform mesopores and the p/p0 of the end of the desorption branch suggests pore blocking effects (i.e., cylindrical mesopores with uniform bodies connected by narrower cylindrical necks of uniform widths). The hysteresis loop of sample PG-c600 displays a different shape expanding from ca. 0.5–0.85 (hence, the average mesopore size is smaller than for GA-c600), and the loop belongs to type H2(a) of IUPAC classification. The steep desorption branch closing the loop at relative pressures of about 0.5-the percolation threshold of N_2 at −196 °C-suggests that the mechanism of desorption from the larger mesopores is controlled by cavitation effects (i.e., the spontaneous nucleation and growth of gas bubbles in the metastable condensed fluid), where large ink-bottle mesopores have access to the external surface through narrow necks smaller than 5–6 nm) [31–33].

In such complex pore systems, the analysis of the PSD is not straightforward due to the complex pore-blocking or cavitation induced evaporation effects. In both cases, the analysis of the adsorption branch of the isotherm can be considered as a good approximation to get a realist distribution of the size of the mesopore bodies. However, in situations of pore blocking/percolation controlled evaporation (sample GA-c600), information about the size of the pore necks can be obtained from the desorption branch. On the contrary, no quantitative information about the neck size can be obtained in the case of cavitation from the analysis of the desorption branch of the N_2 isotherm, as the width of the pore size distribution would be still artificially narrow because the liquid evaporates from both the constrictions and the larger pores simultaneously [31].

Fig. 4 shows the corresponding PSD obtained from the adsorption branch of the isotherms of the samples, where the

Table 1
Carbonization yields, elemental analysis (wt.%), surface pH and surface concentration (at.%) of carbon and oxygen species obtained by XPS of the photopolymerized resins after carbonization at 600 °C.

Sample	GA-c600	PG-c600	DN-c600	BP-c600
Yield after carbonization[a] (wt.%)	9	24	18	11
Initial carbon content[b] (wt.%)	51.6	57.1	74.7	78.9
Carbon[c] (wt. %)	91.6	90.3	92.1	92.5
Oxygen[c] (wt.%)	6.1	7.4	5.0	4.7
Hydrogen[c] (wt. %)	2.3	2.4	2.9	2.8
Surface pH	9.1	8.3	7.3	8.3
Carbon[d] (at. %)	96.1	94.3	95.6	94.5
Oxygen[d] (at.%)	3.9	5.7	4.4	5.5

[a] Yield after the carbonization at 600 °C.
[b] Carbon content used in the synthesis (considering the precursor's formula).
[c] Evaluated from elemental analysis.
[d] Evaluated by fitting the C 1s and O 1s core level peaks of XPS spectra.

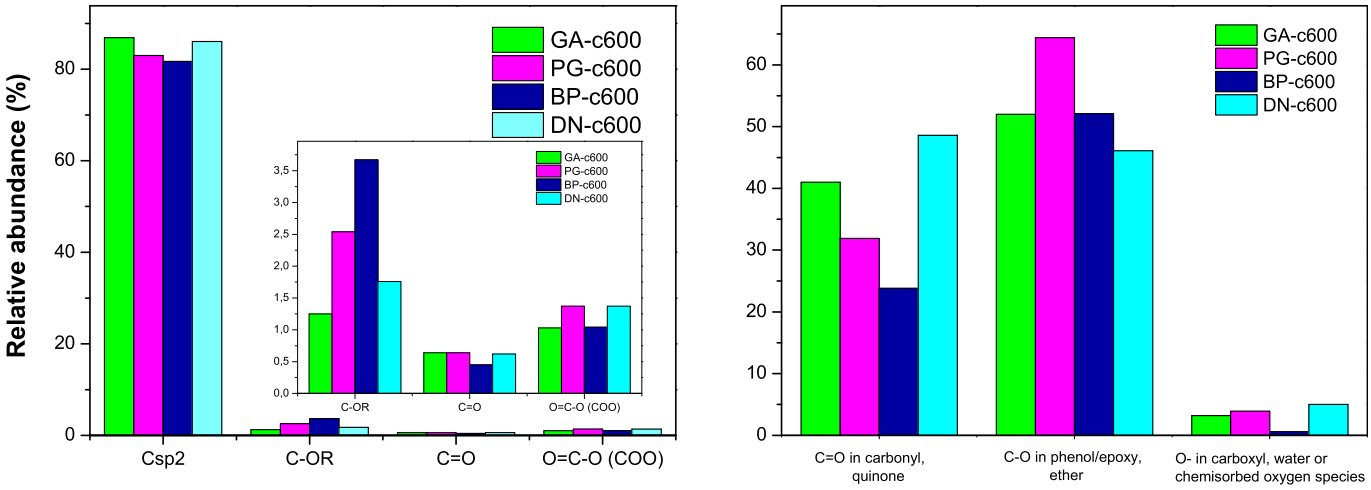

Fig. 3. Relative abundance (%) of carbon (left) and oxygen (right) species in various environments obtained by fitting the C1s and O1s and core level peaks, respectively, of the XPS spectra of the photopolymerized resins after carbonization at 600 °C. (A colour version of this figure can be viewed online.)

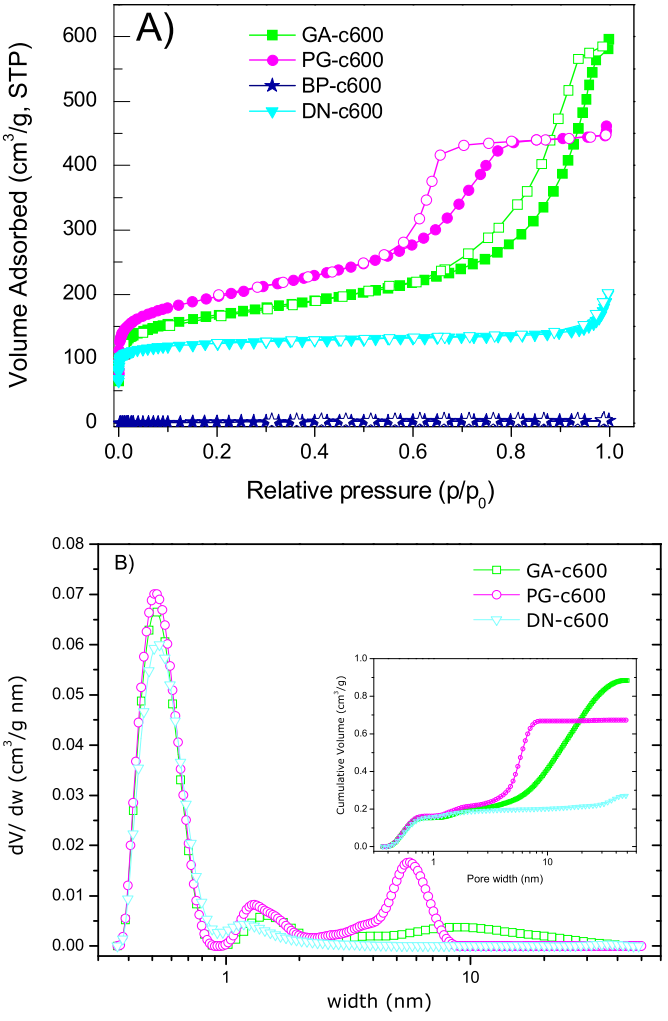

Fig. 4. (A) High resolution N_2 adsorption isotherms at −196 °C of the photopolymerized resins after carbonization (full symbol: adsorption; empty symbol: desorption). (B) Distribution of pore sizes evaluated using the 2D-NLDFT-HS method applied to the adsorption branch of the nitrogen data (inset shows the cumulative pore volume). (A colour version of this figure can be viewed online.)

mesoporosity is cantered at about 10 and 6 nm for GA-c600 and PG-c600, respectively. The narrower distribution of mesopores of PG-c600 vs. GA-c600 and the smaller size of the pores (in average) is in excellent agreement with the analysis obtained from the observation of the gas adsorption isotherms (validating the application of the method for the assessment of the PSD). On the other hand, the analysis of the desorption branch (Fig. S7) showed the narrow distribution of PG-c600 cantered at about 5 nm, due to the cavitation effects, as opposed to the 9 nm for GA-c600 where pore blocking effects apply.

The TEM images revealed marked differences among the samples (Fig. 5). Sample BP-c600 displayed a dense structure composed of rectangular particles of nanometric dimensions, which is in agreement with the low porosity measured for this material by gas adsorption. Samples GA-c600 and DN-c600 show the typical structure of amorphous carbon materials with ill-defined aggregates in disorganized arrangement. In contrast, TEM images of sample PG-c600 showed a rather ordered pattern of well-aligned parallel channels, similar to the ordered hexagonal array of mesopores. TEM images confirmed the pore diameter of ca. 4–5 nm (and a lattice parameter of ca. 10 nm), which is in agreement with the data from N_2 adsorption. Similar textures are typically obtained for solids with long range ordering structures (such as SBA-15, CMK-3 carbons) with hexagonal symmetry [34].

The structural order of the carbons was also investigated by Raman spectroscopy (Fig. 6, Table S2) and X-ray diffraction (Fig. S8). For all the samples the Raman profiles are dominated by the characteristic D-bands and G-bands related to the sp^2 and sp^3

Table 2
Main textural parameters of the carbonized resins (series MM-c600) obtained from gas adsorption data.

Sample	S_{BET} (m^2/g)	V_{PORES}[a] (cm^3/g)	$V_{MICROPORES}$[b] (cm^3/g)	$V_{MESOPORES}$[b] (cm^3/g)	$W_{0,\ CO2}$[c] (cm^3/g)	L[d] (nm)
GA-c600	620	0.89	0.20	0.57	0.19	0.62
PG-c600	720	0.69	0.22	0.46	0.21	0.63
DN-c600	10	0.006	–	–	0.20	0.66
BP-c600	486	0.28	0.19	0.09	0.18	0.64

[a] Evaluated at p/p0 ~ 0.99.
[b] Evaluated from the 2D-NLDFT-HS method applied to N_2 adsorption data.
[c] Narrow micropores volume, evaluated from DR equation applied to CO_2 adsorption data.
[d] Evaluated using the Stoeckli-Ballerini equation applied to CO_2 adsorption data.

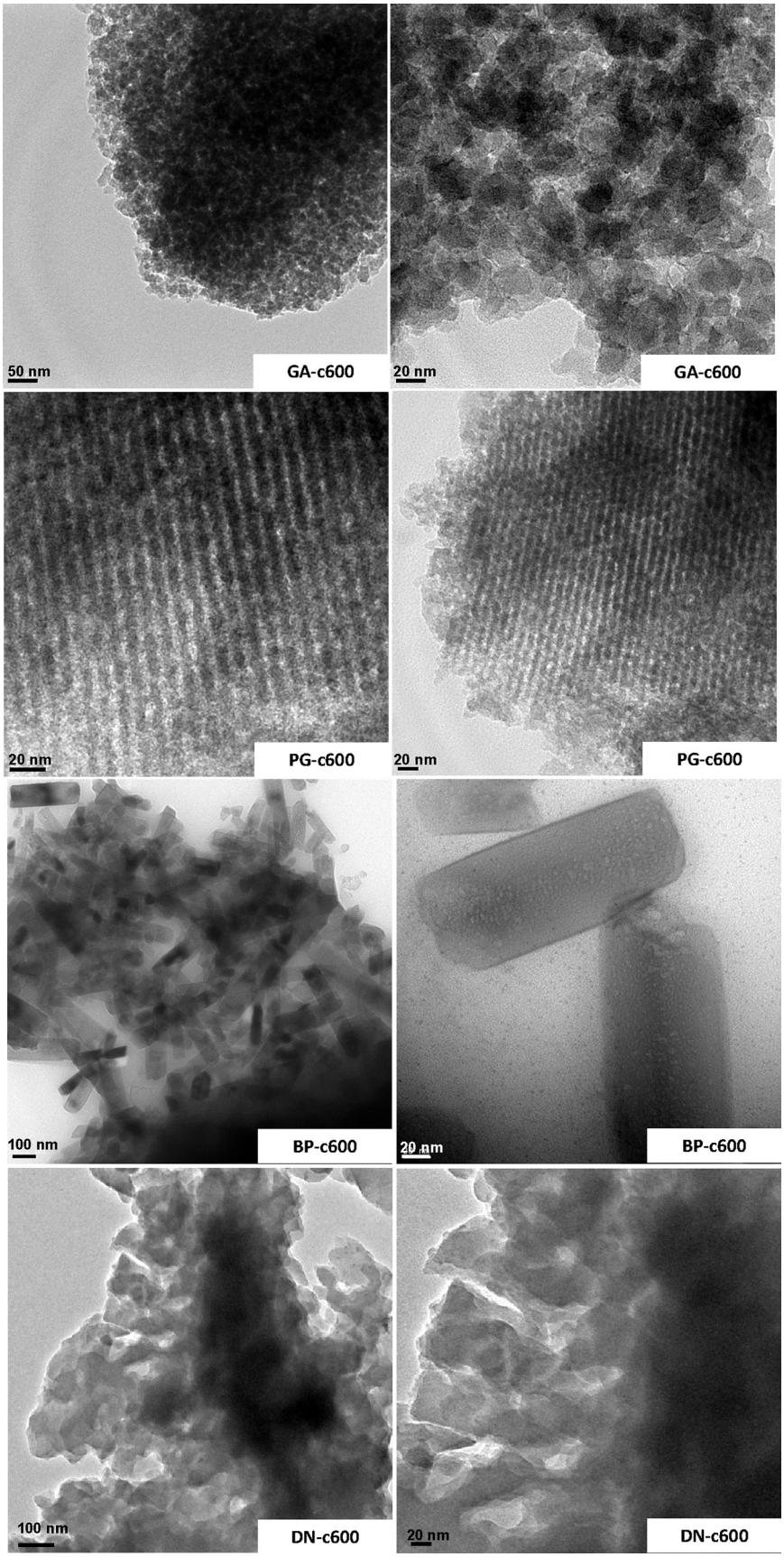

Fig. 5. TEM images of the photopolymerized resins after carbonization at 600 °C.

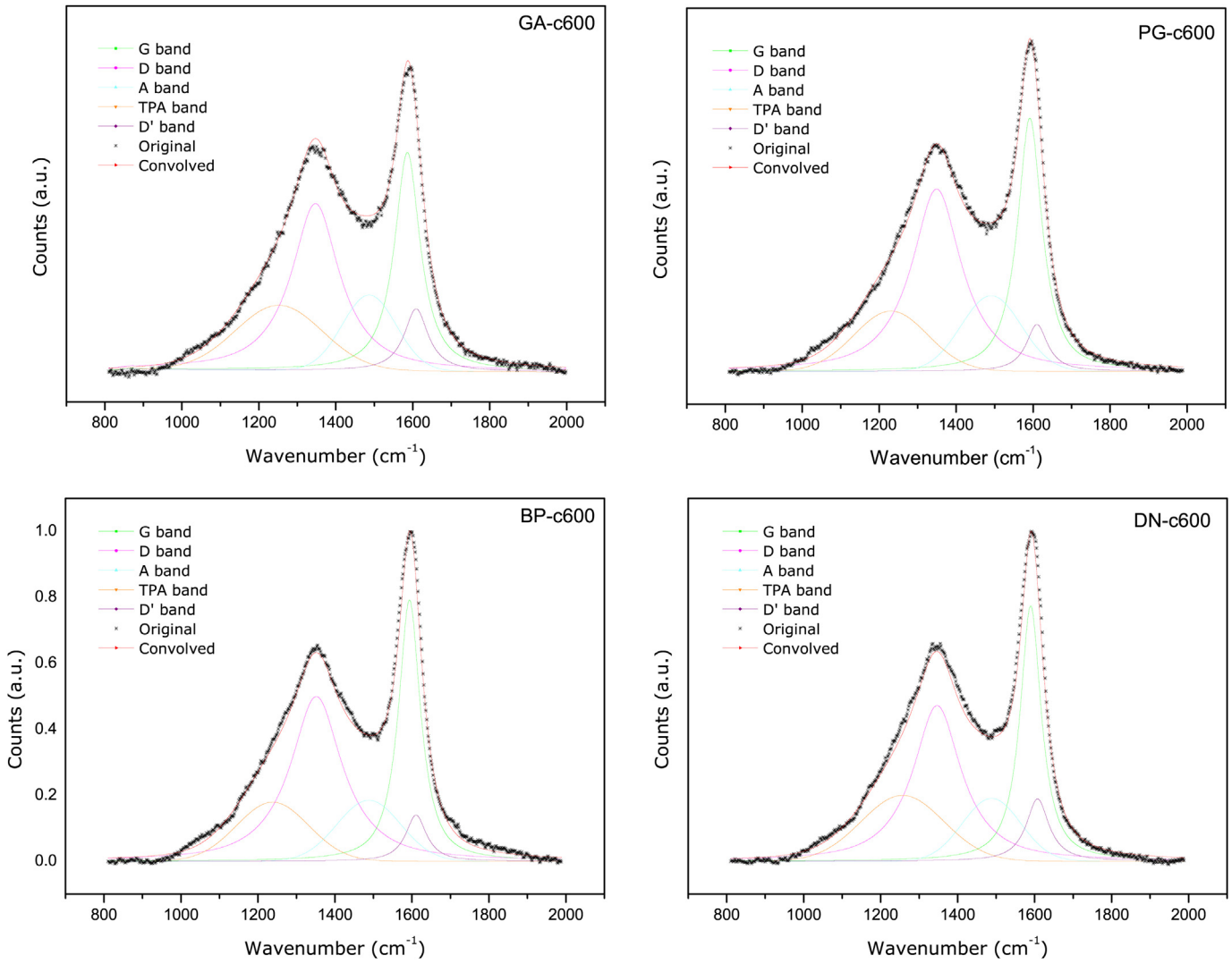

Fig. 6. Raman profiles of the photopolymerized resins after carbonization at 600 °C. (A colour version of this figure can be viewed online.)

content of carbon materials (Fig. 6). The large contribution of the D band in the spectra, indicates that the obtained materials do not present a long-range structural order, but rather features characteristic of disordered carbons [12]. The deconvolution of the first-order spectra allowed a precise evaluation of the I_G/I_D ratio as a measurement of the degree of structural ordering (Fig. 6, Table S2). The Raman spectra were deconvoluted using G, D, D′, A and TPA bands as suggested in the literature for carbon materials [35–37]. The G band observed at 1585-1595 cm^{-1} is assigned to a Raman-allowed E2g resulting from 'in plane' displacement of the carbons strongly coupled in the hexagonal sheets. The position is slightly up-shifted relative to graphite (1580 cm^{-1}), as also seen for other sp^2-dominated carbons.

The D band appearing at ca. 1348 cm^{-1} is due to the lack of long range translation symmetry in disordered carbons. A careful decomposition of the spectra reveals two other additional Gaussian components. A band located at about 1500 cm^{-1} (A band) associated to sp^2-base point-like defects (single and double vacancies in non-hexagonal ring structures) in disordered carbons, and is The TPA band at 1230-50 cm^{-1} attributed to C–C and C=C stretching vibrations of polyene-like and transpolyacetylene-like structures. The variation of the I_D/I_G ratio is a measure of changes in the structural ordering of the carbon network, non-detectable by classical powder X-ray diffraction. Samples showed I_D/I_G values following the trend (Table S2): GA-c600 (0.91) < PG-c600 (0.75) < BP-C600 (0.61) < DN-c600 (0.63), indicating the slightly higher structural order of the later. Nevertheless, all the samples showed the typical fingerprint of carbons with a rather disorganized (turbostratic) structure. This contrasts with the TEM images obtained from PG-c600 showing particles with an ordered pattern with aligned channels; this suggests that the ordered arrangement would correspond to morphological aspects of the particles (as also reported for solids with hexagonal symmetry [34]), rather than to structural order of the carbon matrix.

Useful information concerning the positions of linkage between the aromatic rings of the precursors that gave rise to the formation of the porosity of the carbons was obtained by ^{13}C NMR spectra of the samples. Data representative for PG-c600 and BP-c600 are shown in Fig. 7 (samples were selected given their differences in porosity and similarities in composition and structural order evidenced by XPS and Raman). The spectra of both samples is quite similar, showing a broad intense signal between 100 and 140 ppm corresponding to sp^2 (aromatic and olefinic) carbon and a shoulder at around 151 p.m. typical for C=C–O in an aromatic structures (furan rings or aromatic carbons bearing a hydroxyl group). The main signal between 100 and 140 ppm can be divided into different

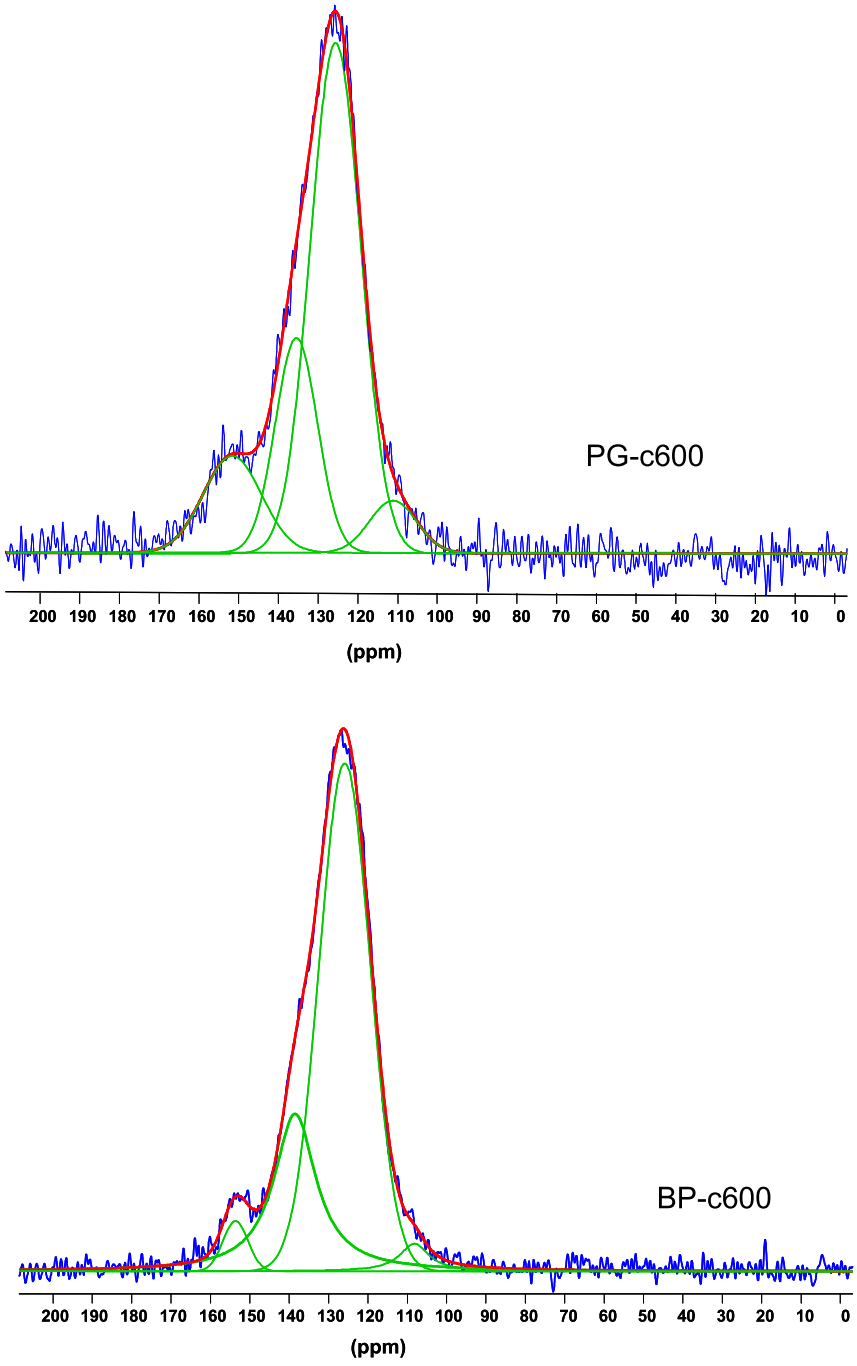

Fig. 7. ^{13}C solid-state NMR spectra of PG-c600 and BP-c600. (A colour version of this figure can be viewed online.)

peaks accounting for carbon atoms in various configurations: i) between 145 and 125 ppm accounting for *ortho*, *para* and *meta* substituted and aromatic carbons, and ii) between 120 and 113 for *ortho*, *para* and *meta* unsubstituted aromatic carbons (assignments are made based on the extensive data in the literature on related materials) [38,39]. No other peaks at higher fields (i.e., chemical shift below 90 ppm) were observed, indicating the negligible contributions of sp^3 +C–H moieties (e.g., aliphatic carbon).

This is in agreement with the high fraction of carbon in sp^2 configuration detected by XPS. The absence of signals around 91 ppm (assigned to unreacted glyoxal) and around 195–200 ppm (assigned to carbon in carbonyl groups, either free or directly attached to the phenol ring) also confirmed that the dialdehyde is fully consumed during the photopolymerization. The contribution of the shoulder at 150 ppm is smaller for BP-c600 (Fig. S9), indicating a higher aromaticity of this sample (lower phenol-ring substitution). Also, the intensity corresponding to unsubstituted carbons compared to that of substituted ring carbons is relatively small for both samples, which is consistent with the highly substituted character of the resins (oxo-aromatic compounds, mainly phenol groups). The peak assigned to the resonances of unsubstituted aromatic carbons has a higher contribution for PG-c600, indicating the higher cross-linking of this sample.

Summarizing, ^{13}C solid-state NMR and gas adsorption data have revealed that the UV exposure of polyhydroxylated benzenes and glyoxal mixtures provokes the cross-linking of the reactants,

obtaining carbon materials with varied micro/mesoporosity depending on the aromatic precursor used. The reaction is sensitized by a colored product likely resulting from the condensation of the precursors, similar to that reported for phenolic resins [40,41]. When the precursors are mixed and exposed to UV light, intermediate species are photogenerated that are able to trigger the phenolic condensation between the precursors and glyoxal at room temperature, likely following a nucleophilic substitution between the hydroxylated compound and the dialdehdyde. The initial substitution reaction between aldehydes and hydroxylated benzenes is usually faster (in a catalyzed medium) than the subsequent condensation reaction between substituted phenol rings. The formed methylolphenols can further condense with other methylol groups to form ether linkages or with the reactive positions on the aromatic ring (unsubstituted positions *ortho* or *para* to the hydroxyl group) to form methylenebridges. Provided that there are enough reactive positions, they become cross-linked in the presence of the dialdehyde and harden to form phenol-like resins. In the case of BP, the photopolymerization occurs, but the resulting material did not show porosity (as in the case of the rest of the aromatic precursor). This could be attributed to the fact that bisphenol A displays a relatively long linear chain, that would allow a less efficient spatial packing of the colloidal aggregates, that would form dense form small clusters of branched polymeric species that would become more unstable in the nucleation regime easily undergoing spinodal decomposition. Consequently, the particles of BP-c600 show a dense structure and close porosity formed of narrow pores. In contrast, GA, PG and DN can assemble together in larger and highly cross-linked clusters, creating a more open porous structure due to the formation of clusters of larger sizes before spinodal decomposition.

Typically, heating or acidifications of the resins are used to promote the cross-linking of the network to form dense, interconnected and porous materials. One of the unique features of this photoassisted synthetic approach herein proposed is the ability to produce a variety of textural features and morphologies and the possibility to control both the structural order and pore size distributions of the obtained carbon materials operating at room temperature by using UV exposure after relatively short times (ca. 60 min of UV exposure).

4. Conclusions

We herein propose a simple and cost effective method for the synthesis of nanoporous carbon materials with varied textural and structural features based on the UV assisted condensation of organic polymeric precursors at room temperature for 60 min. Owing to the specificity of the organic precursors, they react differently upon UV exposure giving rise to resins, the carbonization of which renders nanoporous carbons of hydrophobic nature and varied porosity and morphology. By an adequate choice of the organic precursor, it is possible to control the morphology, structural order and the pore size distributions of the final carbon materials within the full micro/mesoporous range. Photolysis of polyhydroxylated benzenes and glyoxal mixtures triggers the photopolymerization of the reactants at room temperature, likely through a nucleophilic substitution mechanism, which provokes the formation of cross-linked aggregates or clusters that undergo spinodal decomposition. The degree of cross-linking of the reactant is determined by the structure (linear, cyclic) as well as the number of reactive positions (i.e., unsubstituted positions *ortho* or *para* to the hydroxyl moieties and aldehyde group) in the organic precursors. Thus, the linear structure of bisphenol A gave rise to highly branched clusters that harden to form the phenol-like resin in a dense structure with close porosity mainly composed of narrow micropores. On the other hand, the aromatic organic precursors are able to assemble in large cross-linked clusters, creating a more open structure.

One of the unique features of this photoassisted synthetic approach is the ability to produce a variety of morphologies and the possibility to control both the structural order and pore size distributions of the resulting carbon materials. The use of UV light to start the polymerization of the precursors enable to obtain a solid without the need for evaporation of solvents or further thermopolymeration (usually needed in the synthesis of phenolic resins to promote the cross-linking of the network). The future challenge is in controlling the synthesis conditions to achieve nanoporous carbon matrices in a controlled way, and to introduce surface functionalization through the incorporation of photosensitizers groups (heteroatoms and metallic doping) that could be active under different illumination conditions.

Acknowledgments

This study was supported by the European Research Council through a ERC-Consolidator Grant (648161-PHOROSOL) and the Spanish MINECO (grant CTM2014-56770-R).

Appendix A. Supplementary data

Supplementary data related to this article can be found at http://dx.doi.org/10.1016/j.carbon.2017.01.088.

References

[1] S.E. Braslavsky, Glossary of Terms Used in Photochemistry, third ed., 2007, p. 79 (IUPAC Recommendations 2006). Pure and Applied Chemistry.
[2] J.-P. Fouassier, Photoinitiation, Photopolymerization, and Photocuring: Fundamentals and Applications, Hanser Publishers: Distributed by Hanser/Gardner Publications, Munich, 1995.
[3] V. Ramamurthy, S. Kirk, Organic, Physical, and Materials Photochemistry, CRC Press, 2000.
[4] Norman S. Allen, Photochemistry and Photophysics of Polymer Materials, John Wiley & Sons, Inc., 2010.
[5] S. Niu, R. Schneider, L. Vidal, L. Balan, Thioxanthone functionalized silver nanorods as smart photoinitiating assemblies to generate photopolymer/metal nano-objects, Nanoscale 5 (2013) 6538–6544.
[6] L. Balan, V. Melinte, T. Buruiana, R. Schneider, L. Vidal, Controlling the morphology of gold nanoparticles synthesized photochemically in a polymer matrix through photonic parameters, Nanotechnology 23 (2012) 415705.
[7] Carbon nanomaterials, in: Y. Gogotsi, V. Presser (Eds.), Advanced Materials and Technologies, second ed., CRC Press, 2013.
[8] K. Ishizaki, S. Komarneni, M. Nanko, Porous materials, in: R.G. Ford (Ed.), Materials Technology Series, vol. 4, Springer US, Boston, MA, 1998.
[9] W. Xin, Y.H. Song, Mesoporous carbons: recent advances in synthesis and typical applications, RSC Adv. 5 (2015) 83239–83285.
[10] C.D. Liang, Z.J. Li, S. Dai, Mesoporous carbon materials: synthesis and modification, Angew. Chem. Int. Ed. 47 (2008) 3696–3717.
[11] J. Wang, S. Kaskel, KOH activation of carbon-based materials for energy storage, J. Mater. Chem. 22 (2012) 23710–23725.
[12] H. Marsh, F. Rodríguez-Reinoso, Activated Carbon, Elsevier Science & Technology books, Oxford, 2006.
[13] S. Tanaka, A. Doi, N. Nakatani, Y. Katayama, Y. Miyake, Synthesis of ordered mesoporous carbon films, powders, and fibers by direct triblock-copolymer-templating method using an ethanol/water system, Carbon 47 (2009) 2688–2698.
[14] S.A. Al-Muhtaseb, J.A. Ritter, Preparation and properties of resorcinol–formaldehyde organic and carbon gels, Adv. Mater. 15 (2003) 101–114.
[15] A.-H. Lu, D. Zhao, P. O'Brien, H. Craighead, H. Kroto, Nanocasting; RSC Nanoscience & Nanotechnology, 2009. The Royal Society of Chemistry.
[16] C.J. Brinker, G.W. Scherer, Sol-gel Science: the Physics and Chemistry of Sol-gel Processing, Gulf Professional Publishing, 1990.
[17] L. Cao, D.N. Barsic, A.R. Guichard, M.L. Brongersma, Plasmon-assisted local temperature control to pattern individual semiconductor nanowires and carbon nanotubes, Nano Lett. 7 (2007) 3523–3527.
[18] D.D. Kulkarni, S. Kim, A.G. Fedorov, V.V. Tsukruk, Light-induced plasmon-assisted phase transformation of carbon on metal nanoparticles, Adv. Funct. Mater. 22 (2012) 2129–2139.
[19] L. Jia, G.P. Mane, C. Anand, D.S. Dhawale, Q. Ji, K. Ariga, A. Vinu, A facile photo-induced synthesis of COOH functionalized meso-macroporous carbon films

and their excellent sensing capability for aromatic amines, Chem. Commun. 48 (2012) 9029–9031.
[20] Patent Application BFF 14P0494 PP « Procédé de preparation de matériaux » 2014.
[21] J. Jagiello, J.P. Olivier, Carbon slit pore model incorporating surface energetical heterogeneity and geometrical corrugation, Adsorption 19 (2013) 777–783.
[22] J. Jagiello, J.P. Olivier, 2D-NLDFT adsorption models for carbon slit-shaped pores with surface energetical heterogeneity and geometrical corrugation, Carbon 55 (2013) 70–80.
[23] G. Rasines, C. Macias, M. Haro, J. Jagiello, C.O. Ania, Effects of CO_2 activation of carbon aerogels leading to ultrahigh micro-meso porosity, Microp. Mesop. Mater. 209 (2015) 18–22.
[24] M. Thommes, K. Kaneko, A.V. Neimark, J.P. Olivier, F. Rodriguez-Reinoso, J. Rouquerol, K.S.W. Sing, Physisorption of gases, with special reference to the evaluation of surface area and pore size distribution (IUPAC technical report), Pure Appl. Chem. 87 (2015) 1051–1069.
[25] Ullmann's Fine Chemical, 3 Volume Set; Wiley-VCH, John Wiley & Sons, 2014.
[26] P. Shuttleworth, A. Matharu, J.A. Clark, Polysaccharides based porous materials, Ch. 10, in: Polysaccharides Building Blocks, John Wiley and Sons, 2012, p. 271.
[27] T.J. Bandosz, C.O. Ania, Surface chemistry of activated carbons and its characterization. In interface science and technology, in: T.J. Bandosz (Ed.), Activated Carbon Surfaces in Environmental Remediation, vol. 7, Elsevier, 2006, pp. 159–229. Chapter 4.
[28] J.F. Moulder, W.F. Stickle, P.E. Sobol, K.D. Bomben, Handbook of X-Ray Photoelectron Spectroscopy: a Reference Book of Standard Spectra for Identification and Interpretation of XPS Data; Physical Electronics Division, Perkin-Elmer Corporation, 1992.
[29] J. Garrido, A. Linares-Solano, J.M. Martin-Martinez, M. Molina-Sabio, F. Rodriguez-Reinoso, R. Torregrosa, Use of nitrogen vs. Carbon dioxide in the characterization of activated carbons, Langmuir 3 (1987) 76–81.
[30] M. Thommes, K.A. Cychosz, Physical adsorption characterization of nanoporous materials: progress and challenges, Adsorption 20 (2014) 233–250.
[31] J. Landers, G.Y. Gor, A.V. Neimark, Density functional theory methods for characterization of porous materials, Colloids Surfaces A Physicochem. Eng. Aspects 437 (2013) 3–32.
[32] P.I. Ravikovitch, A.V. Neimark, Experimental confirmation of different mechanisms of evaporation from ink-bottle type pores: equilibrium, pore blocking, and cavitation, Langmuir 18 (2002) 9830–9837.
[33] P.A. Monson, Understanding adsorption/desorption hysteresis for fluids in mesoporous materials using simple molecular models and classical density functional theory, Microporous Mesoporous Mater. 160 (2012) 47–66.
[34] M. Impéror-Clerc, P. Davidson, A. Davidson, Existence of a microporous corona around the mesopores of silica-based SBA-15 materials templated by triblock copolymers, J. Am. Chem. Soc. 122 (2000) 11925–11933.
[35] C. Hu, S. Sedghi, A. Silvestre-Albero, G.G. Andersson, A. Sharma, P. Pendleton, F. Rodríguez-Reinoso, K. Kaneko, M.J. Biggs, Raman spectroscopy study of the transformation of the carbonaceous skeleton of a polymer-based nanoporous carbon along the thermal annealing pathway, Carbon 85 (2015) 147–158.
[36] J.N. Rouzaud, A. Oberlin, C. Beny-Bassez, Carbon films: structure and microtexture (optical and electron microscopy, Raman spectroscopy), Thin Solid Films 105 (1983) 75–96.
[37] M.S. Dresselhaus, A. Jorio, A.G. Souza Filho, R. Saito, Defect characterization in graphene and carbon nanotubes using Raman spectroscopy, Philos. Trans. A Math. Phys. Eng. Sci. 368 (2010) 5355.
[38] B. Ottenbourgs, P. Adriaensens, R. Carleer, D. Vanderzande, J. Gelan, Quantitative Carbon-13 solid-state N.m.r. and FT–Raman spectroscopy in novolac resins, Polymer 39 (1998) 5293–5300.
[39] G.E. Maciel, I.S. Chuang, L. Gollob, Solid-state Carbon-13 NMR study of resol-type phenol-formaldehyde resins, Macromolecules 17 (1984) 1081–1087.
[40] A. Gardziella, L.A. Pilato, A. Knop, Phenolic Resins, Springer Berlin Heidelberg, Berlin, Heidelberg, 2000.
[41] L.R.C. Barclay, M.R. Vinqvist, Phenols as antioxidants, in: Z. Rappoport (Ed.), The Chemistry of Phenols, John Wiley & Sons, Ltd, 2003, pp. 839–908.